

Thermal and mechanical properties of (W,Zr)B_{2-z} coatings deposited by RF magnetron sputtering method

Tomasz Mościcki^a, Justyna Chrzanowska-Giżyńska^{a,*}, Rafał Psiuk^a, Piotr Denis^a,
K. Mulewska^b, Łukasz Kurpaska^b, Marcin Chmielewski^c, Maria Wiśniewska^d, Dariusz Garbiec^d

^a Institute of Fundamental Technological Research, Polish Academy of Sciences, Pawińskiego 5B, 02-106 Warsaw, Poland

^b NOMATEN Centre of Excellence, National Centre for Nuclear Research, ul. A. Soltana 7, 05-400 Otwock, Poland

^c Lukaszewicz Research Network, Institute of Microelectronics and Photonics, Center of Electronic Materials Technology, 133 Wolczynska Str, 01-919 Warsaw, Poland

^d Lukaszewicz Research Network – Poznań Institute of Technology, 6 Ewarysta Estkowskiego St., 61-755 Poznań, Poland

ARTICLE INFO

Keywords:

Superhard coatings
Tungsten diboride
Zirconia doping
Magnetron sputtering
Cycling thermal loads
Annealing

ABSTRACT

Magnetron sputtered WB₂ coatings doped with 8, 11 and 16 at.% zirconium were analysed using energy dispersive spectroscopy, X-ray diffraction and nanoindentation under the load of 4, 7 and 10 mN. It has been observed that these coatings crystallize in the α-AlB₂ and ω-W₂B₅ prototype structure. Phenomenon responsible for this is an increase of the zirconium content which causes an increase in the ω-W₂B₅ phase. All the deposited coatings have a hardness of about 45 GPa while Young's modulus drops down from 497 to 480 GPa with increasing zirconium content. Coatings without doping and doped with 16 at.% zirconium were annealed at 650 °C and subjected to cyclic thermal loads using a maximum temperature 600 °C and cooling with a compressed air. It has been observed that addition of zirconium improved coatings phase stability.

1. Introduction

Tungsten borides are distinguished by their high hardness, high melting point, chemical, and thermal stability. This unique combination of properties finds application in the production of high-speed tools, dies (rod drawing), and brake discs. In recent years different tungsten borides compositions were tested. However, the recent research is focused on a tungsten diboride because the results of numerical simulations as well as the experimental data indicate the hardness of this material to be over 40 GPa [1] while maintaining its perfect thermal stability up to 700 °C [2]. Due to the possibility of microstructure formation, the coatings exhibit even better properties in comparison with solid materials [3]. Moreover, WB₂ properties can be enhanced by the addition of Zr [4], Ti [5], Ta [6,7], and N [11]. Recent publication shows that addition of tantalum [6] or titanium [5] to α-WB₂ can improve both strength and fracture toughness in deposited coatings. This effect is related to the improvement of the transformation temperature of the AlB₂-type WB₂ phase.

In this work we decided to focus on the effect of zirconium (Zr) doping on the properties of WB₂ coatings deposited in the magnetron sputtering process. The results of experimental research obtained to date

show the formation of the non-equilibrium α-WB₂ phase [1,7] even though ω-W₂B₅ is more thermodynamically stable [20]. The process of physical vacuum deposition synthesis is responsible for this effect, because this method is known to favor the formation of the point defects such as vacancies which stabilize the non-equilibrium phase. Referring to the results of Moraes' et al. [7,8], one can see that vacancies can be further stabilized by dopants which favor the formation of the phase with negative formation energy. In the case of ZrB₂, formation energy is −0.987 eV [9], so even lower than the formation energy of already investigated TaB₂ (−0.649 eV). In this work our goal is to obtain coatings with a hardness comparable or higher to that of α-WB₂ with improved elastic properties and better thermal stability simultaneously. Reported results suggest that we were able to achieve this via Zr doping of the tungsten diboride.

2. Materials and methods

2.1. Process of magnetron sputtering

The sputtering targets with a diameter of 25.4 mm were produced by spark plasma sintering (SPS) from boron (purity: 95%, APS: 1 μm, Sigma

* Corresponding author.

E-mail address: jchrzan@ippt.pan.pl (J. Chrzanowska-Giżyńska).

<https://doi.org/10.1016/j.ijrmhm.2022.105811>

Received 16 September 2021; Received in revised form 13 December 2021; Accepted 17 February 2022

Available online 24 February 2022

0263-4368/© 2022 Elsevier Ltd. All rights reserved.

Table 1

Weight content of tungsten, zirconium and boron in W/B W/Zr/B powder mixtures used for the preparation of sputtering target.

Stoichiometric composition	Tungsten [g]	Zirconium [g]	Boron [g]
WB _{2.5}	12.202	–	1.795
W _{0.92} Zr _{0.08} B _{2.5}	11.635	0.502	1.861
W _{0.84} Zr _{0.16} B _{2.5}	11.025	1.042	1.931
W _{0.76} Zr _{0.24} B _{2.5}	10.366	1.624	2.007

Aldrich), tungsten (purity: 99.9%, APS: 25 μm , Sigma Aldrich), and zirconium (purity: 99.8%, APS: 250–350 μm , Sigma Aldrich). Powders were mixed for 30 min using a Turbula® T2F shaker-mixer (WAB, Switzerland) in the compositions presented in Table 1. The obtained powder mixtures were SPSed in vacuum using an HP D 25/3 furnace (FCT Systeme, Germany). The SPS process parameters are as follow: sintering temperature: 1800 °C, heating rate: 400 °C/min, holding time: 24 min and compacting pressure: 50 MPa. All targets were composed of a hexagonal WB₂ phase (space group P6₃/mm) and a hexagonal WB₄ phase (space group P6₃/mm). The lattice parameters of both phases remained almost constant in the analysed range of Zr doping and were $a = 2.992 \text{ \AA}$ and $c = 13.933 \text{ \AA}$ for the WB₂ phase and $a = 5.354 \text{ \AA}$ and $c = 6.384 \text{ \AA}$ for the WB₄ phase. They are in good agreement with the theoretical lattice parameters which are as follows: in WB₂ phase $a = 3.016 \text{ \AA}$ and $c = 21.052 \text{ \AA}$, in WB₄ phase $a = 5.360 \text{ \AA}$ and $c = 6.453 \text{ \AA}$. The hexagonal ZrB₂ phase (space group P6/mmm) was observed in the Zr-doped targets (Fig. 1) at 2θ angle of 32.61 and 41.6°, therefore in great agreement with the theoretical position of the (100) and (101) plane of ZrB₂, respectively. The lattice parameters of ZrB₂ phase are $a = 3.171 \text{ \AA}$ and $c = 3.547 \text{ \AA}$ and are consistent with the theoretical parameters of $a = 3.170 \text{ \AA}$, $c = 3.548 \text{ \AA}$. Detailed information on SPS targets can be found in Ref. [4].

Afterwards, each target was mounted in the water-cooled 1-in. magnetron sputtering cathode (Kurt J. Lesker, Germany). The deposition process was performed in a vacuum chamber initially pumped to $2 \cdot 10^{-5}$ mbar and then filled with an argon gas up to the working pressure of $9 \cdot 10^{-3}$ mbar. The gas flow of argon was set to be 19 mL/min. Prior to each deposition, the target was sputtered for 5 min in order to ensure its clean surface and stable sputtering conditions. During all experiments, power supplied to the magnetron cathode was maintained at the level of 50 W. Films were deposited for 45 min on Si (100) (Institute of Electronic Materials Technology, Poland) and tungsten carbide G15 substrates. Substrate holder was heated up to 540 °C and positioned 40 mm in front of the target. The deposited coatings were about 1 μm thick.

2.2. Annealing and cycling temperature changes

Two types of coatings (WB_{2-z} and W_{0.76}Zr_{0.16}B_{2-z}) deposited on the tungsten carbide substrate were subjected to the heat treatment and the cyclic temperature changes.

Stability of both nanostructure and mechanical properties of the deposited coatings were studied after annealing at temperature of 650 °C inside the vacuum chamber (PREVAC) pumped to a pressure of $2 \cdot 10^{-5}$ mbar. Samples were held at constant temperature for an hour and after the annealing, cooled down for 120 min to a temperature of 100 °C.

Described tests of cyclic temperature changes were carried out in the heating-cooling system ShockTherm (PESS Company), using a maximum temperature 600 °C and cooling with a compressed air stream to room temperature. The temperature was controlled by thermocouples placed just above the samples. Individual heating-cooling cycle took approximately 180 s, while the typical course of the process is presented in Fig. 2. Changes in the structure and evolution of layer properties were analysed after 10 and 50 heating-cooling cycles.

2.3. Characterization

The surface microstructure and chemical composition were investigated using Scanning Electron

Microscope – SEM (JEOL JSM-6010Plus) equipped with an energy sensitive detector (EDS). In order to get the most reliable values of boron content the accelerating voltage was set to be 5 kV, according to Ref. [12]. Moreover, the system was calibrated with the use of

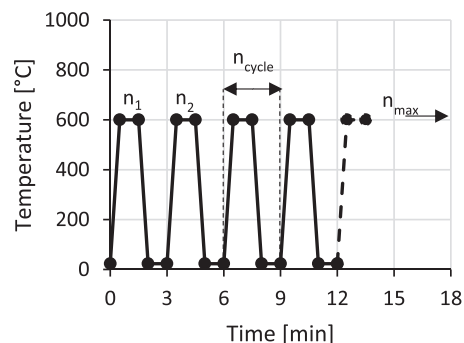


Fig. 2. Schematic view of the heating-cooling cycle.

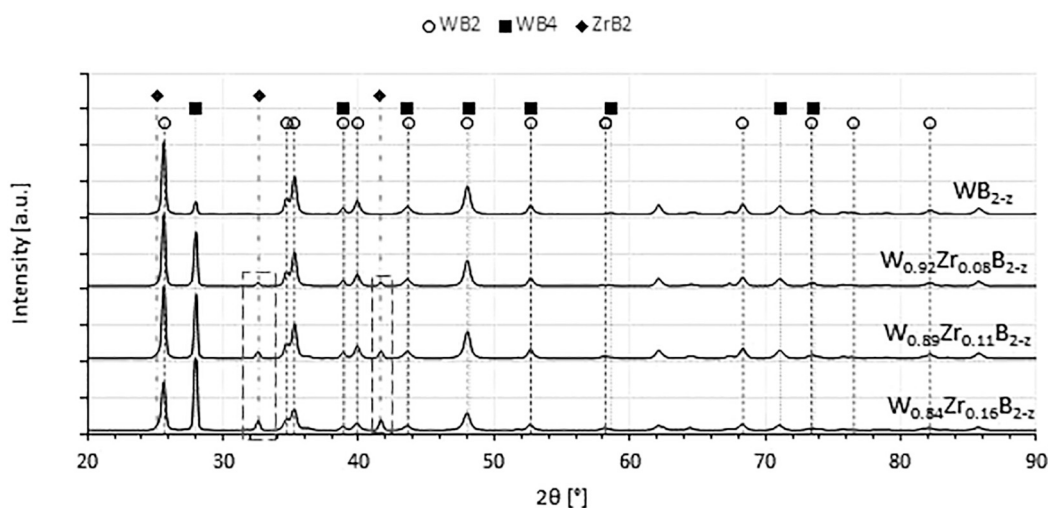


Fig. 1. XRD diffractogram of WB_{2.5} and W_{1-x}Zr_xB_{2.5} SPS targets. Marked with dashed lines area shows growing intensity of the diffraction patterns, which indicates growing content of ZrB₂ phase.

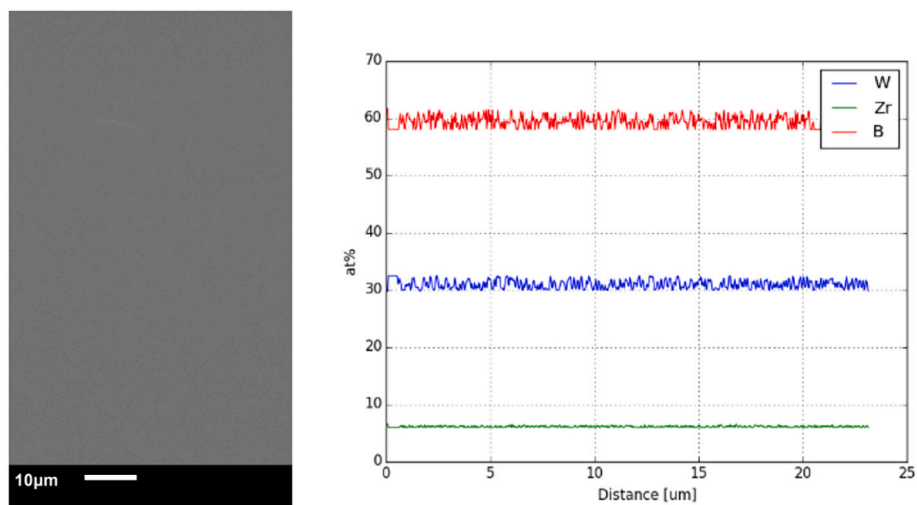


Fig. 3. a) SEM image of WB_{2-x} , b) EDS line scanning analysis of the coating deposited from the $W_{0.76}Zr_{0.24}B_{2-z}$ target.

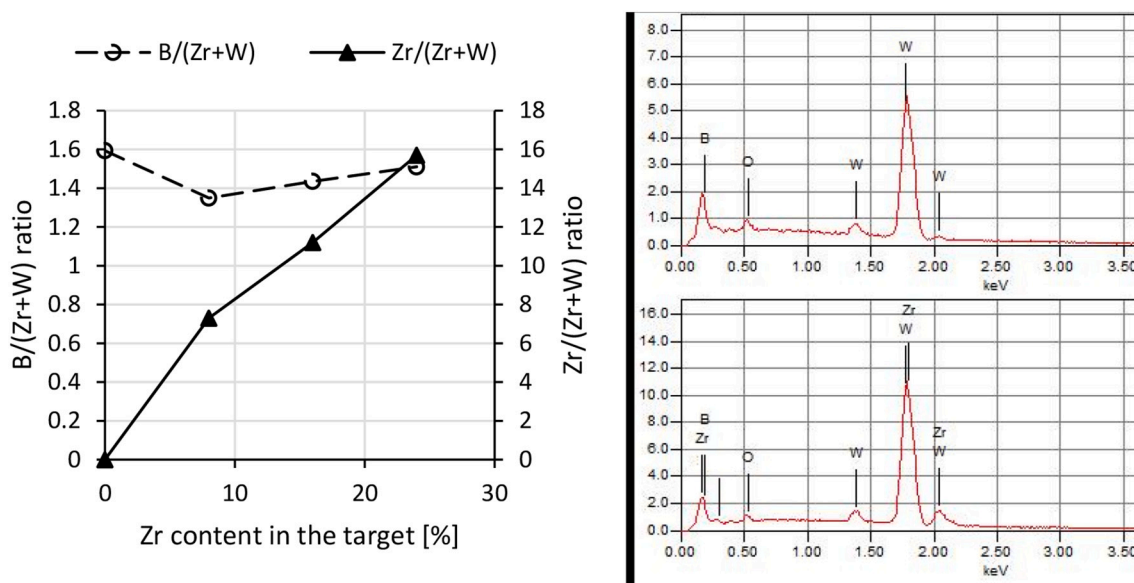


Fig. 4. Chemical composition of the deposited coatings a) $B/(Zr + W)$ and $Zr/(Zr + W)$ concentration, b) an example of EDS spectrum of the coating deposited from $WB_{2.5}$ (top) and $W_{0.76}Zr_{0.24}B_{2.5}$ target (bottom).

commercially available target W_2B_5 (purity 99.9%, Huizhou Tian Yi Rare material Co. Ltd). It should be explained that the authors are aware of the uncertainties in boron measurement with EDS, which are related to the proximity of the boron and carbon peaks as well as carbon contamination. However, precise measurement of boron and tungsten at the same time is difficult with other techniques such as XPS as well. This is partially related to the accuracy of the calibration [15,16]. The crystal structure and phase composition of deposited layers were characterized by X-Ray Diffractometer (Bruker D8 Discover, $\lambda = 1.5418 \text{ \AA}$) system. Measurements were made in 2θ scan mode, with the *sample fixed at a constant angle of incidence at 8°* . In this configuration, it was possible to avoid signal from the substrate while maintaining high intensity of the signal originating primarily from the studied coating. Rietveld refinement was used for the phase analysis of the targets and the coatings.

2.4. Mechanical properties

Nanoindentation analyses were performed at room temperature using NanoTest Vantage (Micro Materials) system. Measurements were

performed with Berkovich-shaped diamond indenter. The geometry of the indenter tip, so called Diamond Area Function, was calculated for each load and used when calculating mechanical parameters. Each indentation has been repeated 12 times and the measurements were made in the line with the distance of $50 \mu\text{m}$ from each other. To minimize the effect of the substrate, the hardness and elastic modulus values were calculated based on the average data obtained at depths of about 100 nm (indentation load of 7 mN). The goal of this is to (i) ensure that the maximum indentation depth is not bigger than $1/10$ of the coating thickness, thus minimizing substrate effect [13] and (ii) to measure hardness in load independent region [14], thus minimizing deformation created by the preceding indent.

3. Results and discussion

All the deposited coatings were smooth with a mean square roughness of $12 \pm 5 \text{ nm}$. No debris or delamination was observed, see Fig. 3a. Performed SEM-EDS analysis indicate that chemical elements composing $W_xZr_{1-x}B_{2-z}$ coatings after magnetron sputtering were

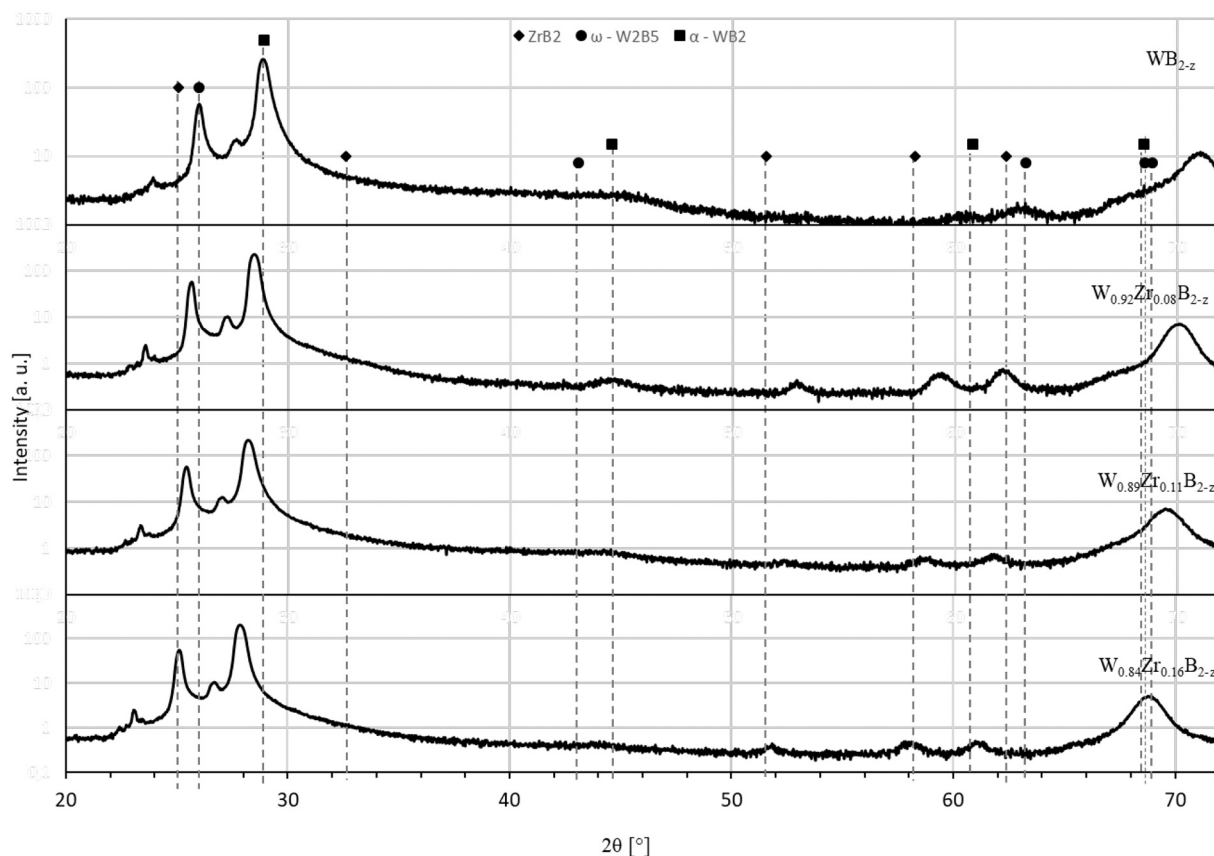


Fig. 5. Structural evolution of the as-deposited $W_{1-x}Zr_xB_{2-z}$ coatings with increasing Zr content ($x = 0, 0.08, 0.11, 0.16$). The standardized 2θ -peak positions of ω - W_2B_5 ($a = 2.983 \text{ \AA}$, $c = 13.879 \text{ \AA}$) [18], α - WB_2 ($a = 3.020$, $c = 3.050$) [19], and AlB_2 -type- ZrB_2 ($a = 3.170 \text{ \AA}$, $c = 3.548 \text{ \AA}$) are marked with circle, square and filled rhombus symbols, respectively.

homogeneously distributed in the entire surface of the coating (see Fig. 3b). The boron content $B/(Zr + W)$ is in the range of 62.5–74.6 at.% (1.36–1.59, see Fig. 4) which means that boron decreased by 36–46% compared to the target composition. A decrease of light elements has already been observed, e.g. in Ref. [3,17]. This phenomena may be related to the plasma scattering of light boron atoms (10.81 u) into heavy tungsten atoms (183.84 u). As a result of this, lower amount of boron seems to reach the substrate.

In the coatings deposited from zirconium-doped targets, the zirconium content dropped up to 34% in the comparison to initial target composition. The decrease in zirconium content, as in the case of boron, is predicted to be due to scattering of the zirconium atoms (91.224 u) on

the tungsten atoms. Therefore, similar as previously described phenomena can be observed, resulting with lower Zr% then predicted.

The XRD diffractogram of the deposited coatings revealed main diffraction peaks at 2θ ranging from about 24° to 31° , see Fig. 5a. In the case of WB_{2-z} coating the peak positioned at 28.9° originates from the (001) plane of hexagonal AlB_2 -type WB_2 (α - WB_2) while the peak positioned at 26° is derived from the (004) plane of hexagonal MoB_2 -type WB_2 (ω - W_2B_5). Detailed deconvolution of XRD diffractogram leads to the determination of cell parameters as well as phase composition. The α - WB_2 phase is characterized by the following lattice parameters $a = 2.96 \text{ \AA}$ and $c = 3.089 \text{ \AA}$. At the same time the ω - W_2B_5 phase has the lattice parameters $a = 3.076 \text{ \AA}$, $c = 13.684 \text{ \AA}$. It should be explained that

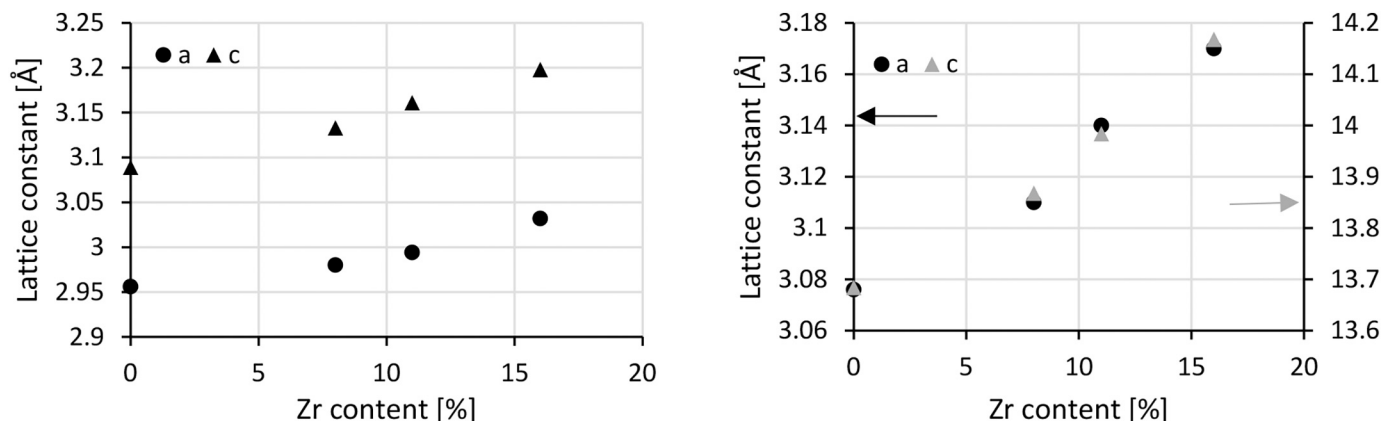


Fig. 6. The effect of Zr content on the lattice parameters a) α - WB_2 , b) ω - W_2B_5 . Triangle and circle stands for a and c lattice constant, respectively.

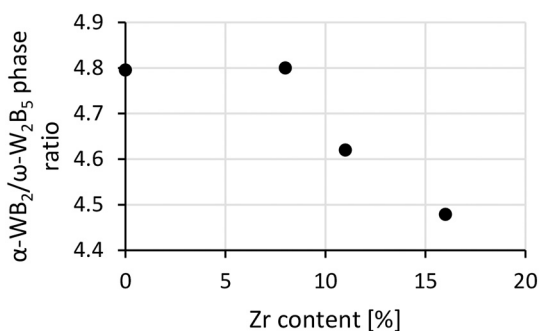


Fig. 7. The effect of Zr content on the phase composition of the deposited coating.

Table 2

. Overview of the phases observed in the $W_{1-x}Zr_xB_{2-z}$ coatings.

Composition of the coating	Lattice constants of the as deposited coating	Phase composition of the coating after 1 h annealing	Phase composition after 50 shocks
WB_{2-z}	$\alpha-WB_2$: a = 2.96 Å, c = 3.09 Å $\omega-W_2B_5$: a = 3.08 Å, c = 13.68 Å	$\alpha-WB_2$: a = 2.96 Å, c = 3.08 Å $\omega-W_2B_5$: a = 3.08 Å, c = 13.78 Å	$\alpha-WB_2$: a = 2.96 Å, c = 3.11 Å $\omega-W_2B_5$: a = 3.08 Å, c = 13.78 Å
$W_{0.92}Zr_{0.08}B_{2-z}$	$\alpha-WB_2$: a = 2.98 Å, c = 3.13 Å $\omega-W_2B_5$: a = 3.11 Å, c = 13.87 Å	-	-
$W_{0.89}Zr_{0.11}B_{2-z}$	$\alpha-WB_2$: a = 2.99 Å, c = 3.16 Å $\omega-W_2B_5$: a = 3.14 Å, c = 13.98 Å	-	-
$W_{0.84}Zr_{0.16}B_{2-z}$	$\alpha-WB_2$: a = 3.03 Å, c = 3.2 Å $\omega-W_2B_5$: a = 3.17 Å, c = 14.17 Å	$\alpha-WB_2$: a = 3.05 Å, c = 3.22 Å $\omega-W_2B_5$: a = 3.20 Å, c = 14.21 Å	$\alpha-WB_2$: a = 3.05 Å, c = 3.24 Å $\omega-W_2B_5$: a = 3.21 Å, c = 14.21 Å
Theoretical $\alpha-WB_2$ phase	Space group P6/mmm: a = 3.020 Å, c = 3.050 Å	-	-
Theoretical $\omega-W_2B_5$	Space group P6 ₃ /mmc: a = 2.983 Å, c = 13.879 Å	-	-

the theoretical parameters are as follows: a = 3.020, c = 3.050 [19] and a = 2.983 Å, c = 13.879 Å [18], respectively. The $\alpha-WB_2$ to $\omega-W_2B_5$ ratio is 4.8 and both phases have similar crystallite size of 37 ± 2 nm (calculated on the basis of Scherrer formula [21]). In the XRD diffractogram, apart from narrow diffraction lines, a broad diffraction line at 2θ between 22° and 46° was observed. This data indicates the presence of the amorphous phase.

In the case of Zr-doped coatings, the amorphous phase decreases, and the remaining diffraction lines (related to $\alpha-WB_2$ and $\omega-W_2B_5$) are shifted towards smaller 2θ angles. Observed shift (towards smaller angles) increases with increasing Zr content. The deconvolution of XRD diffractograms showed that experimentally obtained lattice parameters (both a and c) increase with increasing Zr content, see Fig. 6. Moreover, the $\alpha-WB_2$ to $\omega-W_2B_5$ ratio decreases with Zr, see Fig. 7. Reported behaviour of doped WB_{2-z} coating has been already observed by Moraes et al. [7]. It was indicated that the shift in diffraction lines is related to boron vacancies in WB_2 lattice and the formation of a new phase, in our case this is the W-Zr-B phase. Finally, obtained results point to the conclusion that the crystalline size of $\alpha-WB_2$ and $\omega-W_2B_5$ phases does not change significantly with increasing Zr content and is 30 and 40 nm, respectively. Overview of the phases observed in the $W_{1-x}Zr_xB_{2-z}$ coatings is presented in Table 2.

The formation of non-equilibrium α and ω phases [20] has already been observed in Ref. [7,23]. As in the case of the coatings described in this work, studied by those two teams W-B coatings showed a boron deficiency in relation to the formed phases. Boron deficiency can be related to the coating deposition method. For example, PVD methods are known to promote the incorporation of point defects such as vacancies during crystal growth. Moreover, it has been already shown in Ref. [7,24] that both the boron defects and the doping (contributing formation of the compound having very negative energy of formation) increasing the ω phase stability. The formation energy of ZrB_2 is -0.987 eV, so very negative. This is even lower than the formation energy of TaB_2 (-0.649 eV) which was analysed by Moraes et al. [7].

In the next step, detail nanomechanical investigation has been performed. The tests were made with loads of 4, 7 and 10 mN and show that the plastic depth increases linearly with the load. The reported results indicates that conducted studies are made in a load-independent region, which suggest that developed plastic deformation under the indenter tip originates only from the coating, without the impact of the bulk material, see Fig. 8a. One can see that all the tested coatings do not show an effect of pop-in on the loading region. Therefore, one can expect that up to the indentation load of 10 mN, crack initiation and propagation do not occur [22]. However, with an indentation load above 7 mN, small pop-out effect was observed. This is particularly visible for the WB_{2-x} system, see Fig. 8a,b. The observed phenomenon may be related to two phenomena (i) the delamination of the coating from the substrate or (ii) temperature difference between indenter tip and the specimen. One should explain, that the samples were tested after 24 h from the

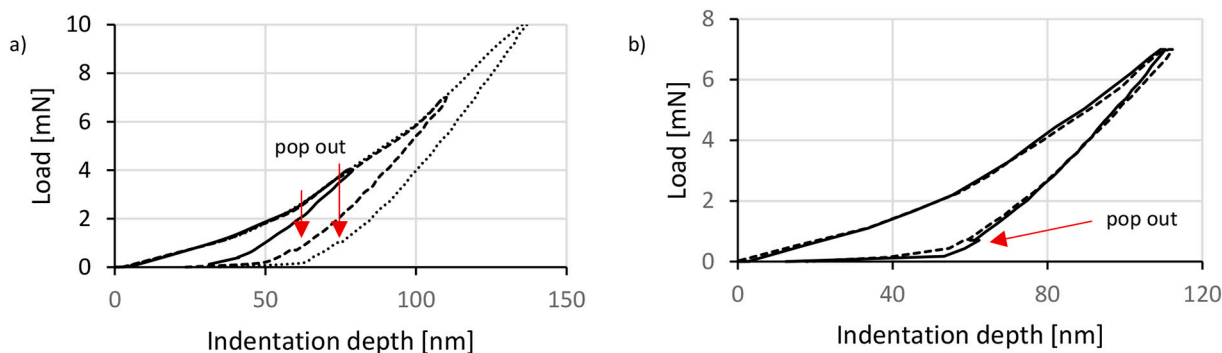


Fig. 8. Load-displacement curves of a) WB_{2-x} coating under maximum load of 5, 7 and 10 mN, b) WB_{2-z} (solid line) and $W_{0.76}Zr_{0.16}B_{2-z}$ (dotted line) under the maximum load of 7 mN. Pop-out effect can be observed in the WB_{2-z} unloading curves.

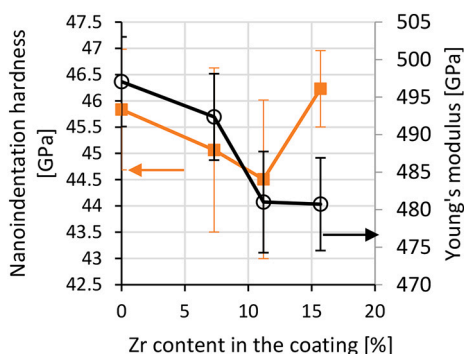


Fig. 9. Nanoindentation hardness and Young's modulus of WB_{2-z} coatings with different Zr content. Circles stands for Young's modulus, squares stands for hardness.

installation in the machine, i.e. any temperature differences should be removed by then.

Mechanical properties of the coatings were compared for the indentation load of 7 mN. This was to avoid the maximum indentation depth exceeding 10% of the coating thickness. It was observed, that in the whole composition range, hardness of the deposited coatings did not

change significantly (it varies from 44.5 ± 1.6 to 46.2 ± 1.6 GPa – see Fig. 9 line with rectangles). However, with increasing Zr content, especially after reaching 10% level, the Young modulus drops down from 497 ± 11 to 480 ± 13 GPa, see Fig. 9 – line with circles.

The WB_{2-z} and $W_{0.76}Zr_{0.16}B_{2-z}$ coatings after 1 h annealing in vacuum at the temperature of 650°C did not delaminate and their roughness remained the same as before the annealing. Recorded XRD diffractograms of WB_{2-z} shows a shift of the main XRD peak α - WB_2 (001) towards the higher 2θ angles (see Fig. 10). This phenomenon indicates the compressive stress component parallel to the sample surface. Another consequence of WB_{2-z} coating annealing is a significant reduction in ω - W_2B_5 (it drops from $\sim 17\%$ to 2%). In the case of the $W_{0.76}Zr_{0.16}B_{2-z}$ coating, the diffractogram did not change. Taking into account high boron deficiency, presented results indicates that (i) α phase field is extended to lower boron contents than ω phase and (ii) Zr stabilize α phase. Similar results were obtained for Ta doping [7].

After annealing, the hardness of the WB_{2-z} coating increased from 45.8 ± 0.6 to 48.3 ± 3.4 GPa, and the Young modulus drops from 497 ± 12 to 481 ± 17 GPa. However, reported result is within the accuracy range of the measurement. The pop-out effect is no longer observed in the unloading curve, see Fig. 11. This can be related to the reduction of internal strains and well thermally stabilized specimen. The mechanical properties of $W_{0.76}Zr_{0.16}B_{2-z}$ appear to be constant after annealing at

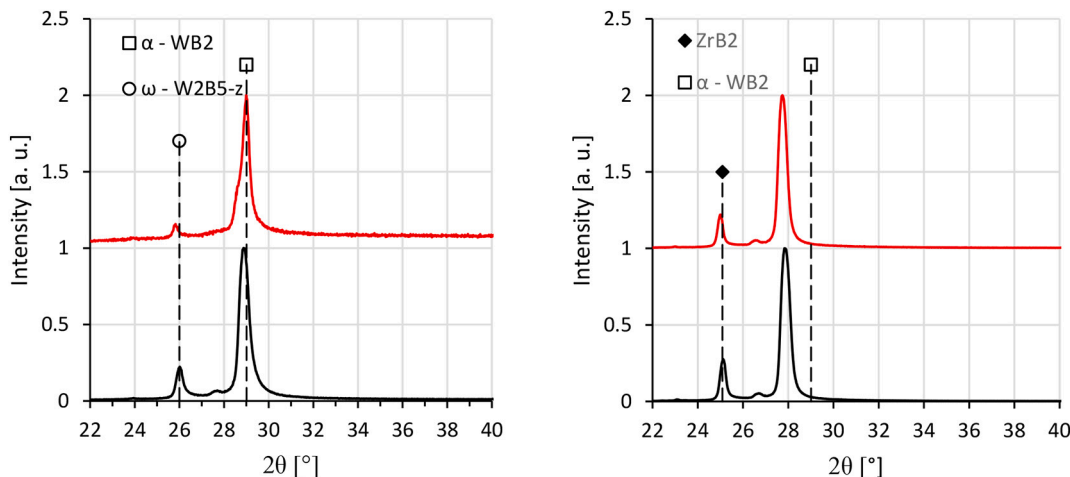


Fig. 10. XRD diffractogram of WB_{2-z} (left) and $W_{0.76}Zr_{0.16}B_{2-z}$ (right) as deposited (black line) and after 1 h vacuum annealing at 650°C (red line). Dotted line stands for theoretical standardized 2θ -peak positions of ω - W_2B_5 , α - WB_2 and ZrB_2 . (For interpretation of the references to colour in this figure legend, the reader is referred to the web version of this article.)

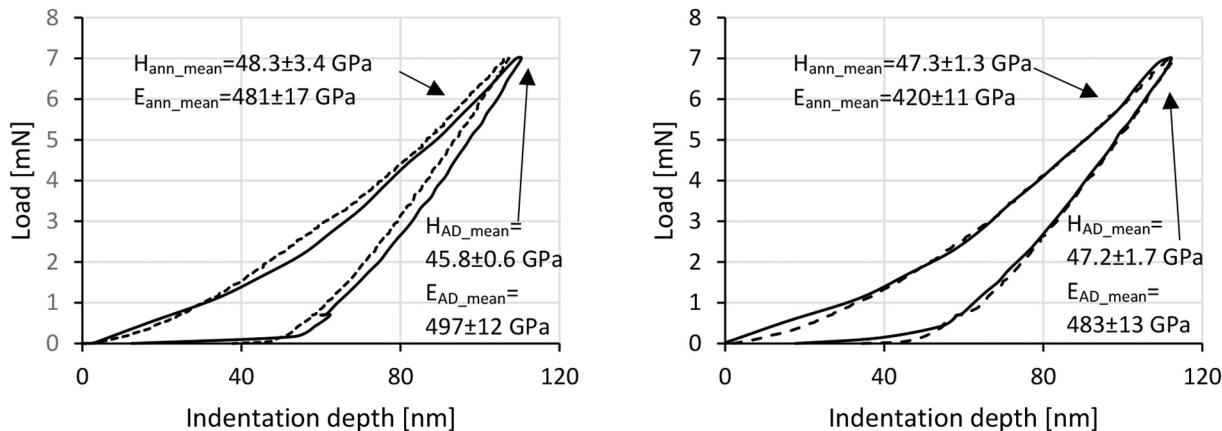


Fig. 11. Load-displacement curves of coatings as deposited (solid line) and after an hour vacuum annealing at 650°C (dashed line) a) WB_{2-z} , b) $W_{0.76}Zr_{0.16}B_{2-z}$. H_{AD_mean} – average hardness from 10 measurements of as deposited coating, H_{ann_mean} – average hardness from 10 measurements of the coating after an hour vacuum annealing at 650°C .

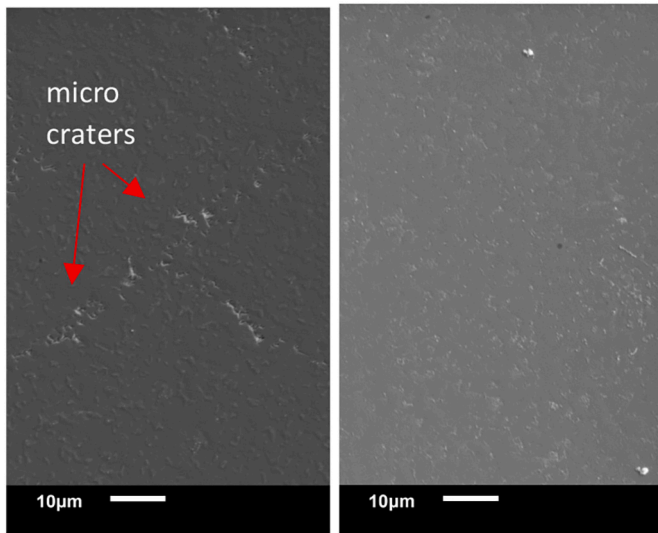


Fig. 12. SEM images of WB_{2-z} (left) and $W_{0.76}Zr_{0.16}B_{2-z}$ after 50 thermal shocks (right).

650 °C.

The influence of cyclic thermal loading on the properties of the deposited coatings seems to be more significant than the annealing process itself. First, the surface roughness increased to 35 ± 7 and 21 ± 5 nm for the WB_2 and $W_{0.76}Zr_{0.16}B_{2-z}$ coatings, respectively. A change in surface quality was also observed in the SEM images, where the appearance of a preferential grain growth can be observed. Moreover, in the case of WB_{2-z} coating, micro craters with a diameter of up to 2 µm were noticed, see Fig. 12.

The XRD diffractograms of WB_{2-z} coating after 50 thermal shocks

show an increase in the ratio of ω - W_2B_5 to α - WB_2 phase and the presence of ω - W_2B_5 diffraction lines other than (004), see Fig. 13. It has been calculated that ω - W_2B_5 phase increases from 17 up to 27%. In the case of the $W_{0.76}Zr_{0.16}B_{2-z}$ coating, new diffraction lines originating from the ω - W_2B_5 phase were also observed, but the content of the above-mentioned phase has not changed significantly. The XRD diffractograms of both tested coatings show a shift of the main diffraction lines towards smaller diffraction angles. This phenomenon indicates a uniform increase in strain which may result from the difference in thermal expansion coefficient between the substrate and the layer.

The different results reported after heating and thermal shocking may originate from the rate of change of the heat load. Fig. 2 shows the operation of the furnace, while the actual temperature changes on the surface of the layer will be much more abrupt (the thin layer will heat up and cool down rapidly). Due to the lower thermodynamic stability of the α phase, it is expected that this phase is reduced in the case of the WB_{2-z} coating. For the Zr-doped coatings, an alpha stabilization effect can be observed, which is in line with the simulations presented in Ref. [7].

The nanoindentation test shows that the heating-cooling cycles led to an increase in Young's modulus of about 50% for both WB_{2-z} and $W_{0.76}Zr_{0.16}B_{2-z}$ coatings (58 and 53%, respectively), see Fig. 14. The hardness increases by 28 and 17%, respectively, for the WB_{2-z} and $W_{0.76}Zr_{0.16}B_{2-z}$ coatings. The increase in hardness and Young modulus may be due to residual stresses after thermal shocks. This subject will be further developed in the up-coming contribution of this group. Series of spherical nanoindentation tests with different indenter sizes are planned to be performed. This will allow us to calculate stress-strain curves for these systems and ultimately will lead to calculation of different mechanical parameters like: shear stress, yield point, UTS or hardening exponent.

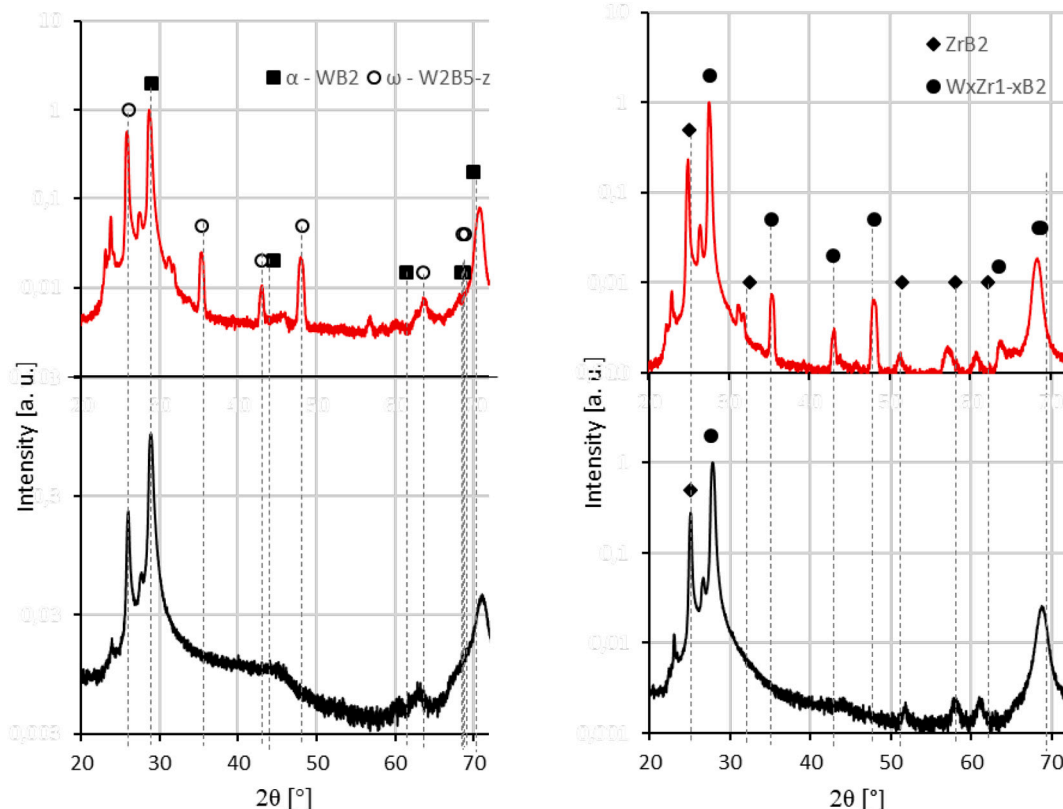


Fig. 13. XRD diffractogram of WB_2 (left) and $W_{0.76}Zr_{0.16}B_2$ (right) as deposited (solid line) and after 50 shocks (dashed line). A base 10 log scale is used for the Y axis.

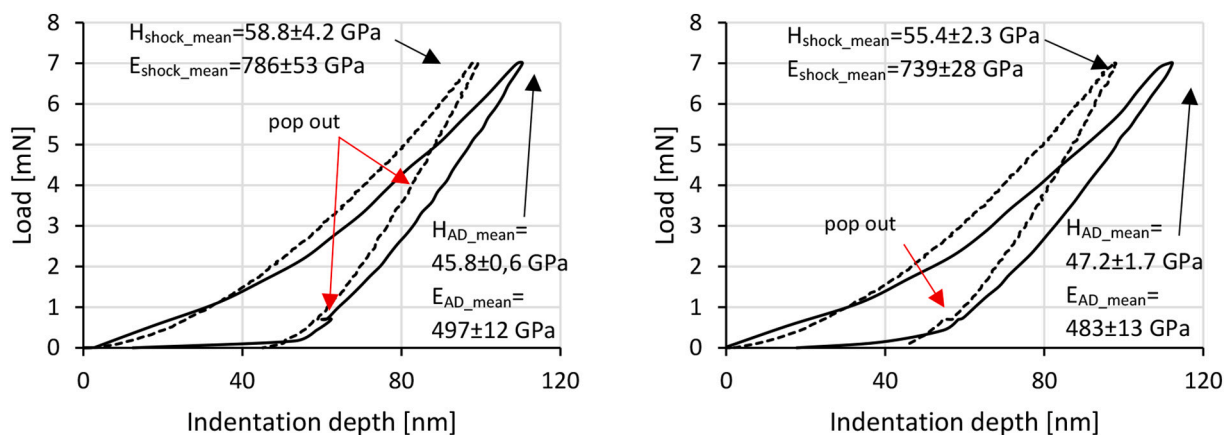


Fig. 14. Load-displacement curves of the coatings as deposited (solid line) and after 50 thermal shocks (dashed line) a) WB_{2-zr} , b) $W_{0.76}Zr_{0.16}B_{2-zr}$. $H_{AD,mean}$ – average hardness from 10 measurements of as deposited coating, $H_{shock,mean}$ – average hardness from 10 measurements of the coating after 50 shocks.

4. Conclusions

The experimentally obtained lattice parameters of WB_{2-zr} coating are in good agreement (for α - WB_2 and ω - W_2B_5) with previously reported lattice parameter increase with increasing Zr content. Taking into account boron concentration it can be stated that all deposited coatings have boron vacancies. According to the numerical simulations and available experimental data, it has been noticed that α -phase field is extended to lower boron contents than ω phase. Moreover, Zr doping contribute formation of the compound having very negative energy of formation which stabilize α phase.

From the mechanical point of view, the deposited coatings are superhard showing hardness above a 44.5 GPa. W-Zr-B coatings have a hardness similar to WB_{2-zr} and at the same time have a lower Young modulus. Thermal tests (annealing and cycling thermal loads) point to the conclusion that Zr doped coatings are characterized by better mechanical properties and have higher thermal stability. In addition to that, these coatings show to be less prone to cracking and have a lower Young's modulus. In the case of cycling thermal loads the hardness and Young's modulus of coatings grow due to thermal residual stresses.

Declaration of Competing Interest

The authors declare that they have no known competing financial interests or personal relationships that could have appeared to influence the work reported in this paper.

Acknowledgement

This work was co-financed by the National Science Centre (NCN, Poland) under project no. UMO-2017/25/B/ST8/01789.

This work was co-financed by the National Centre for Research and Development (NCBR, Poland) under project no. TECHMATSTRATEGIII/0017/2019.

References

- [1] Y.M. Liu, C.L. Jiang, Z.L. Pei, H. Lei, J. Gong, C. Sun, Microstructure and properties of AlB_2 -type WB_2 thin films deposited by direct-current magnetron sputtering, *Surs. Coat. Technol.* 245 (2014) 108–116.
- [2] Yan-Ming Liu, Tong Li, Feng Liu, Zhi-Liang Pei, Thermal stability of WB_2 and W-B-N deposited by magnetron sputtering, *Acta Metall. Sin.* 32 (2019) 136–144.
- [3] J. Chrzanowska, Ł. Kurpaska, M. Giżyński, J. Hoffman, Z. Szymański, T. Mościcki, Fabrication and characterization of superhard tungsten boride layers deposited by radio frequency magnetron sputtering, *Ceram. Int.* 42 (10) (2016) 12221–12230.
- [4] D. Garbiec, M. Wiśniewska, R. Psiuk, P. Denis, N. Levintant-Zayonts, V. Leshchynsky, R. Rubach, T. Mościcki, Zirconium alloyed tungsten borides synthesized by spark plasma sintering, *Archives of civil and Mechanical Engineering* 21 (37) (2021).
- [5] T. Mościcki, R. Psiuk, H. Slomińska, N. Levintant-Zayonts, D. Garbiec, M. Pisarek, P. Bazarnik, S. Nosewicz, J. Chrzanowska-Giżyńska, Influence of overstoichiometric boron and titanium addition on the properties of RF magnetron sputtered tungsten borides, *Surf. Coat. Technol.* 390 (2020), 125689-1-12.
- [6] C. Fuger, B. Schwartz, T. Wojcik, V. Moraes, M. Weiss, A. Limbeck, A. Macauley, O. Hunold, P. Polcik, D. Primetzhofer, P. Felfel, P.H. Mayrhofer, H. Riedl, Influence of Ta on the oxidation resistance of WB_{2-zr} coatings, *J. Alloys Compounds* 864 (2021), 158121.
- [7] V. Moraes, C. Fuger, V. Paneta, D. Primetzhofer, P. Polcik, H. Bolvardi, M. Arndt, H. Riedl, P.H. Mayrhofer, Substoichiometry and tantalum dependent thermal stability of α -structured W-Ta-B thin films, *Scr. Mater.* 155 (2018) 5–10.
- [8] V. Moraes, H. Riedl, C. Fuger, P. Polcik, H. Bolvardi, D. Holec, P.H. Mayrhofer, Ab initio inspired design of ternary boride thin films, *Sci. Rep.* 8 (2018) 9288.
- [9] M. Maździarz, T. Mościcki, New zirconium diboride polymorphs – first principles calculations, *Materials* 13 (13) (2020) 3022-1-13.
- [10] Y.M. Liu, T. Li, F. Liu, Z.L. Pei, Thermal stability of WB_2 and W-B-N films deposited by magnetron sputtering, *Acta Metall. Sin.* 32 (136) (2019) 136–144.
- [11] J. Berlin, Analysis of boron with energy dispersive x-ray spectrometry, *Imaging Microsc.* 13 (2011) 19–21.
- [12] J. Chen, S.J. Bull, On the factors affecting the critical indenter penetration for measurement of coating hardness, *Vacuum* 83 (2009) 911.
- [13] J. Chrzanowska-Giżyńska, P. Denis, S. Woźniacka, Ł. Kurpaska, Mechanical properties and thermal stability of tungsten boride films deposited by radio frequency magnetron sputtering, *Ceram. Int.* 44 (16) (2018) 19603–19611.
- [14] G. Greczynski, L. Hultman, C 1s peak of adventitious carbon aligns to the vacuum level: dire consequences for material's bonding assignment by photoelectron spectroscopy, *ChemPhysChem* 18 (2017) 1507–1512.
- [15] G. Greczynski, L. Hultman, Reliable determination of chemical state in x-ray photoelectron spectroscopy based on sample-work-function referencing to adventitious carbon: Resolving the myth of apparent constant binding energy of the C 1s peak, *Appl. Surf. Sci.* 451 (2018) 99–103.
- [16] O.V. Sobol, Influence of deposition conditions and annealing temperature on phase composition and structure of W-B system ion-plasma condensates, *Funct. Mater.* 13 (3) (2006) 387–392.
- [17] Powder Diffraction File 04–007-1000, International Center for Diffraction Data, 2011.
- [18] Powder Diffraction File 04–003-6624, International Center for Diffraction Data, 2011.
- [19] X.Y. Chen, X.Q. Chen, D.Z. Li, Y.Y. Li, Computational materials discovery: the case of the W-B system, *Acts Cryst.* C70 (2014) 81–103.
- [20] P. Scherrer, *Göttinger Nachrichten Gesell* 2, 1918, p. 98.
- [21] B. Bor, D. Giuntini, B. Doménech, M.V. Swain, G.A. Schneider, Nanoindentation-based study of the mechanical behavior of bulk supercrystalline ceramic-organic nanocomposites, *J. Eur. Ceram. Soc.* 39 (2019) 3247–3256.
- [22] R. Hahn, V. Moraes, A. Limbeck, P. Polcik, P.H. Mayrhofer, H. Euchner, Electron-configuration stabilized (W, ADB2) solid solutions, *Acta Mater.* 174 (2019) 398–405.
- [23] H. Euchner, P.H. Mayrhofer, H. Riedl, F.F. Klimashin, A. Limbeck, P. Polcik, S. Kolozsvari, Solid solution hardening of vacancy stabilized $Ti_{x}W_{1-x}B_2$, *Acta Mater.* 101 (2015) 55–61.